scientific reports

OPEN

Existence of La-site antisite defects in LaMO₃ ($M = Mn$, Fe, and Co) predicted with many-body diffusion quantum Monte Carlo

Tom Ichibha[1,2]✉, Kayahan Saritas[1], Jaron T. Krogel[1], Ye Luo[3], Paul R. C. Kent[4] & Fernando A. Reboredo[1]✉

The properties of LaMO₃ (M: 3*d* transition metal) perovskite crystals are significantly dependent on point defects, whether introduced accidentally or intentionally. The most studied defects in La-based perovskites are the oxygen vacancies and doping impurities on the La and M sites. Here, we identify that intrinsic antisite defects, the replacement of La by the transition metal, M, can be formed under M-rich and O-poor growth conditions, based on results of an accurate many-body ab initio approach. Our fixed-node diffusion Monte Carlo (FNDMC) calculations of LaMO₃ (M = Mn, Fe, and Co) find that such antisite defects can have low formation energies and are magnetized. Complementary density functional theory (DFT)-based calculations show that Mn antisite defects in LaMnO₃ may cause the *p*-type electronic conductivity. These features could affect spintronics, redox catalysis, and other broad applications. Our bulk validation studies establish that FNDMC reproduces the antiferromagnetic state of LaMnO₃, whereas DFT with PBE (Perdew–Burke–Ernzerhof), SCAN (strongly constrained and appropriately normed), and the LDA+*U* (local density approximation with Coulomb *U*) functionals all favor ferromagnetic states, at variance with experiment.

The LaMO₃ (M: 3*d* transition metal) perovskites display remarkable features such as superconductivity[1], spin crossovers[2,3], magnetic transitions, and giant magneto resistance[4–6], and the transition metal atoms also provide redox catalytic ability[7]. Beyond the basic science interests in perovskites, their properties are exploited for various applications, including gas sensors[8,9], thermal sensors[2], sub-micrometer magnetic field sensors[10], photocatalysts, catalytic combustion[11], air batteries[12], magnetic read heads, and magnetic memory cells[13].

More interestingly, perovskites can be grown on top of each other via pulsed laser deposition (PLD) and molecular beam epitaxy (MBE)[14,15]. These growth methods allow the fabrication of artificial materials that combine the properties of the individual building blocks with additional effects that result from the interfaces and strain caused by lattice mismatch. For example, strain affects the magnetism[16], electronic conductivity[17], ferroelectricity[18], carrier density[17], and oxygen vacancy concentration[19]. Interestingly, 2D superconductivity is observed at the two types of interfaces of LaAlO₃/SrTiO₃ and LaTiO₃/SrTiO₃[20,21]. The relative lower temperatures in PLD and MBE facilitates the formation of defects as a result of departures of the stoichiometry or limited annealing times. Because defects are well known to alter the magnetic, electronic, and chemical properties of perovskites, their characterization is key to understanding this family of materials and the composite materials

¹Materials Science and Technology Division, Oak Ridge National Laboratory, Oak Ridge, TN 37831, USA. ²School of Information Science, Japan Advanced Institute of Science and Technology, Asahidai 1-1, Nomi, Ishikawa 923-1292, Japan. ³Computational Sciences Division, Argonne National Laboratory, Argonne, IL 60439, USA. ⁴Computational Sciences and Engineering Division, Oak Ridge National Laboratory, Oak Ridge, TN 37831, USA. ✉email: ichibha@icloud.com; reboredofa@ornl.gov

derived from them. At equilibrium, the formation energy of defects determines their relative abundance. However, outside this regime, the relative abundance of defective structures also depends on growth kinetics. Defects with high formation energies will be difficult to form even out of equilibrium. Therefore, the formation energy of defects is a key indicator of their occurrence during natural or artificial growth.

For general ABO_3 perovskites, defects are theoretically possible on any of the atomic sites and in defect complexes. In La-based perovskites, a strong focus has been on the formation energy of the oxygen vacancies because these play an important role in the oxygen reduction reaction[22], oxygen evolution reaction[23], and ionic conduction[24,25]. However, in non-La-based perovskites, such as $YAlO_3$ and $LuAlO_3$, both Y and Lu antisite defects have been predicted[26]. Similarly, DFT calculations predicted that Ni impurities in $BaZrO_3$ occupy the A-site under Ni-rich condition[27]. Experiments also found that Y impurities, B-site dopants in $BaZrO_3$, occupy the A-site as well in the Y richer phase[28]. These examples raise the question as to the extent La-site antisite defects are relevant in $LaMO_3$ perovskites.

Transition metal oxides, including perovskites, are notoriously challenging to current density functional theory (DFT) approximations[29] because strong static and dynamic electronic correlations and self-interaction errors are present at the partially occupied d shells[30]. These errors are compounded for defects that involve transition metals. Accordingly, these materials and their defects are important targets of quantum many-body methods, such as fixed-node diffusion Monte Carlo (FNDMC), that account for electronic correlations and avoid the self-interaction error[31,32]. These methods can be applied to defective supercells and to the ideal bulk solids, making them well-suited to modeling transition metal oxides in general[33–50].

In this paper, we study the formation energy of antisite defects and oxygen vacancies in $LaMO_3$ (M = Mn, Fe, and Co) using FNDMC. We establish for $LaMnO_3$ and $LaFeO_3$ that the formation energy of antisite defects is low enough to form the defects under M-rich and O-poor chemical conditions. However, in $LaCoO_3$, the formation energy of antisite defects is higher for each type of growth conditions studied here. We also show that the antisite defects, as well as the oxygen vacancies, significantly affect the properties of La perovskites. The predicted partial density of states (PDOS) suggests that the antisite defect formation may contribute to the p-type electronic conductivity in $LaMnO_3$ and may narrow the band gap of $LaFeO_3$ and $LaCoO_3$. In addition, we study the magnetic energy order of the non-defective perovskite crystals. Because even the magnetic ground state is still controversial for some perovskites, we determine the magnetic ground state prior to conducting the defect studies. For $LaMnO_3$ and $LaFeO_3$, FNDMC corroborates the experimental antiferromagnetic (AFM) ground state, but the ground state of pristine $LaCoO_3$ remains controversial[16].

The rest of the paper is organized as follows: In "Calculation details" section, we explain how the point defect formation energies are evaluated, including the details of the DFT and FNDMC calculations. In "Results and discussion" section, we discuss the magnetic state of non-defective perovskite crystals. We also discuss the defect formation energies and how the point defects affect electronic conductivity. This work is summarized in "Conclusion" section.

Calculation details

Formation energy of defects.
The formation energies of oxygen vacancy V_O and intrinsic transition metal antisite defects on the La site M_{La} (M = Mn, Fe, and Co) were evaluated in the neutral state by using the following equations:

$$\Delta E(V_O) = E_{V_O} - E_{bulk} + \mu_O, \tag{1}$$

$$\Delta E(M_{La}) = E_{M_{La}} - E_{bulk} + \mu_{La} - \mu_M. \tag{2}$$

Here, E_{bulk} is the total energy of perovskite supercells with no defects, E_{V_O} is an isolated oxygen vacancy, $E_{M_{La}}$ is an isolated antisite defect, and μ_X is the chemical potential of the atomic species X. The formation of charge-neutral oxygen vacancy reduces the neighboring cations. The influence of charge-neutral antisite defect formation on the neighboring ions is discussed in "Atomic distortions around the antisite defect" section. The effects of electron and hole doping are discussed in the supplemental information (SI). The chemical potential (μ_X) and the defect formation energies ($\Delta E(V_O)$ and $\Delta E(M_{La})$) for different equilibrium states are characterized by the solids or gases present during growth. The calculated total energies for the materials were used to determine the chemical potentials to simulate several equilibrium states and are listed in Table 1.

Relaxation of defective and bulk structures.
The Vienna Ab Initio Simulation Package (VASP)[67] was used to relax the atomic positions. The total energy and orbital eigenenergies convergence criteria for the self-consistent field (SCF) process were both 1×10^{-5} eV/simulation cell. The atomic positions were relaxed until the maximum residual force was less than 0.01 eV/Å. We found that the defect formation energy does not significantly change when the structure is altered to the one obtained with a different functional choice (details available in the SI). The lattice vectors were fixed at the reference values listed in Table 1. For $LaCoO_3$, we used the same calculation settings as our previous work[16]. To calculate the chemical potentials and cohesive or formation energies of bulk structures, the atomic positions were also fixed at the reference data values in Table 1. For $LaMnO_3$ and $LaFeO_3$, we used the Perdew–Burke–Ernzerhof (PBE) functional[68] to relax the atomic positions of both bulk and defective structures. The core electrons were replaced using the projector augmented wave (PAW) method[69]. The plane-wave cutoff energy was 520 eV, which converged the total energy of $LaMnO_3$ within 14 meV/atom. The k-mesh spacing was smaller than 0.50 Å^{-1}, which converged the total energy of $LaMnO_3$ within 2.4 meV/atom. The same calculation settings were used to obtain the $LaMnO_3$, $LaFeO_3$, and $LaCoO_3$

Formula	Space group	Lattice constants (Å)	Magnetic state	Supercell size	
O_2	–	$d = 1.24$ (molecule)	–	–	
$La_2O_3^1$	$C2/m$	$a = b = 3.93, c = 6.15^{52}$	NM	16	(80 atoms)
$LaMnO_3$	$Pnma$	$a = 5.54, b = 5.75, c = 7.69^{53}$	AFM-A[54]	4	(80 atoms)
MnO	$Fm\bar{3}m$	$a = b = c = 4.49^{55}$	AFM-A[2]	40	(80 atoms)
MnO_2	$P4_2/mnm$	$a = b = 4.36, c = 2.88^{54}$	AFM-A[54]	13	(78 atoms)
$LaFeO_3$	$Pnma$	$a = 5.56, c = 7.85^{56}$	AFM-G[57]	4	(80 atoms)
Fe	$Im\bar{3}m$	$a = b = c = 2.87^{58}$	FM	64	(64 atoms)
FeO	$Fm\bar{3}m$	$a = b = c = 4.334^{59}$	AFM-A[2]	36	(72 atoms)
Fe_2O_3	$R\bar{3}c$	$a = b = 5.04, c = 13.75^{60}$	AFM[61]	8	(80 atoms)
$La_2O_3^3$	$Ia\bar{3}$	$a = b = c = 11.40^{62}$	NM	Extrap.[4]	
Co	$P6_3/mmc$	$a = b = 2.47, c = 4.02^{63}$	FM	Extrap.[4]	
CoO	$F\bar{4}3m$	$a = b = 3.20, c = 7.70^{64}$	AFM[64]	Extrap.[4]	
Co_3O_4	$Fd\bar{3}m$	$a = b = c = 8.05^{65}$	FM	Extrap.[4]	
$LaCoO_3$	$R\bar{3}c$	$a = 5.36, b = 5.44, c = 7.62,$ $\alpha = 89.97°, \beta = 88.83°, \gamma = 89.79°$ [66]	AFM-G[66]	Extrap.[4]	

Table 1. List of compounds used to calculate the chemical potentials in each equilibrium state. This table summarizes the lattice constants, the magnetic state, and the supercell size as number of primitive cells and atoms. (^{a} For $LaMnO_3$ and $LaFeO_3$ results; ^{b} The energy differences between different AFM structures of the rock-salt type MnO were calculated to be within 50 meV per formula unit by DFT[51]. This energy scale is significantly small compared with the energy scale of point defects formation: the choice of the spin structure would not be significant for the point defects formation energies; ^{c} For $LaCoO_3$ results; ^{d} The total energy was evaluated by the size extrapolation. See the SI for the details).

AFM and FM energy differences. The cohesive or formation energies of the bulk systems listed in Table 1 were calculated using PBE[68] and strongly constrained and appropriately normed (SCAN) functionals[70].

FNDMC calculations' details. We performed FNDMC calculations with the high-performance QMC-PACK code[71,72] with the Nexus workflow management software[73]. We used the Slator-Jastrow-type trial wave functions[74]. The Jastrow factor consisted of one-, two-, and three-body terms. The orbitals of the Slater determinants were obtained with the local density approximation with Coulomb interaction potential (LDA+U) method[30]. Further details of the LDA+U calculations are written in the next subsection. The time step was $dt = 0.01$ a.u.$^{-1}$, and the associated errors were 5 meV/atom for $LaMnO_3$ and $LaFeO_3$[54,75] and less than 20 meV/atom for $LaCoO_3$[16]. The target population of walkers was 2000 or larger for our main results (the SI discusses a few exceptions). We used twist-averaged boundary conditions and size extrapolation to estimate the one- and two-body finite size effects (details in the SI). For $LaFeO_3$, E_{V_O} and E_{bulk} in Eq. (1) were taken from our previous FNDMC results[75].

Tuned LDA+U trial wave function. We used the Quantum ESPRESSO package[76] to run the LDA+U calculations. We used the norm conserving pseudopotentials[54,75,77], whose accuracy has been verified in our previous works[54,75,77]. The cutoff energy was 350 Ry, which converged the total energy of $LaCoO_3$ within 1 meV/atom. The k-mesh size was identical to the twist-averaging mesh size (details in the SI). The energy convergence criterion for the SCF process was 5×10^{-6} Ry or smaller. The Hubbard U contribution was applied to the $3d$ electrons of Mn, Fe, and Co. We optimized the U value for Mn (Fe) to minimize the FNDMC total energy of the bulk $LaMnO_3$ ($LaFeO_3$): $U_{opt} = 3$ eV for Mn and 6 eV for Fe. We optimized the U value for Co to minimize the FNDMC total energy of every bulk system: $U_{opt} = 6$ eV for $LaCoO_3$ and Co and $U_{opt} = 5$ eV for CoO and Co_3O_4. We consistently used the U_{opt} values for our LDA+U calculations throughout the paper. We also used LDA+U with the optimal U values to obtain the PDOS of the perovskites because the FNDMC tuning of DFT+U has been reported to improve the reliability of DFT to study physical properties[40,78,79].

Results and discussion
Cohesive or formation energies and energy differences of magnetic states given by FNDMC and DFT.
The total energies of the materials listed in Table 1 were calculated to obtain the chemical potentials, μ_{La}, μ_M, and μ_O, for different chemical equilibrium conditions. The chemical potentials were used to calculate the defect formation energies with Eqs. (1) and (2). To verify the results, the calculated cohesive energies were compared with the available experimental data[24,80,82–89] (Table S1 in the SI). The differences between calculated and experimental cohesive energies are shown in Fig. 1. The experimental and FNDMC numerical values are listed in Table 1 in the SI. To quantitatively assess the reliabilities of different methods, the mean squared deviations (MSD) were calculated from the experimental data for the cohesive energies. The MSDs were 0.046(4) (eV/atom)^2 for FNDMC, 0.158 (eV/atom)^2 for PBE, and 0.562 (eV/atom)^2 for SCAN: FNDMC gave the lowest MSD. Because the experimental cohesive energies were not found for Co_3O_4 and $LaCoO_3$, we alternatively

3

	Expt.	FNDMC	PBE	SCAN
Co_3O_4	1.33[80]	1.28 (1)	1.00	1.06
$LaCoO_3$	2.55[81]	2.63 (1)	2.23	2.64
MSD	–	0.004 (1)	0.112	0.045

Table 2. Experimental and calculated formation enthalpies (eV/atom) of Co_3O_4 and $LaCoO_3$. The last row indicates the mean of the squared deviations (MSD) from the experimental values.
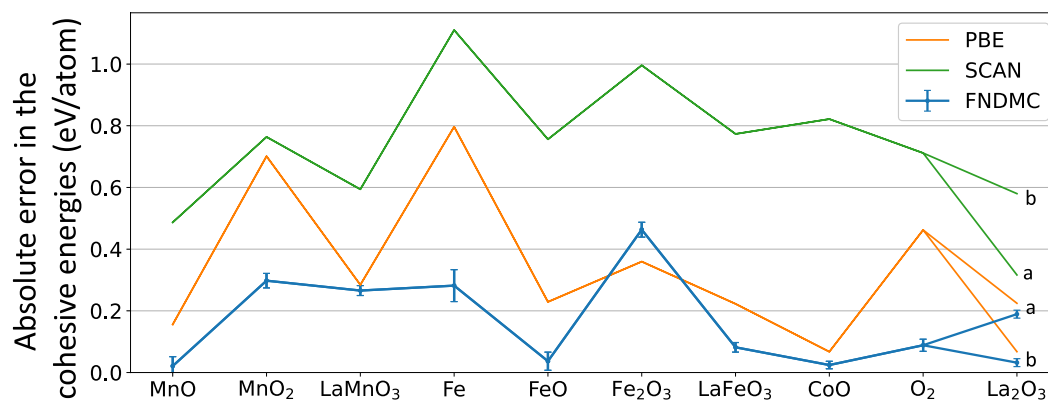

Figure 1. Cohesive energies of the different compounds used to evaluate the chemical potentials in this study compared with experimental data (zero value). a: For $LaMnO_3$ and $LaFeO_3$ results. b: For $LaCoO_3$ results.

Perovskite	PBE	SCAN	LDA+U	FNDMC
$LaMnO_3$	+ 0.02	+ 0.07	+ 0.10	− 0.15 (2)
$LaFeO_3$	− 0.16	− 0.08	− 0.23	− 0.08 (1)
$LaCoO_3$	+ 0.50	− 0.18	− 0.37	− 0.27 (2)[16]

Table 3. Total energy difference (eV/f.u.) between AFM and FM states of $LaMnO_3$, $LaFeO_3$, and $LaCoO_3$: the total energy of the AFM state minus that of the FM state. Negative values indicate greater AFM stability.

compared the formation energies in Table 2: FNDMC reproduced the experimental values significantly better than the DFT approximations that were considered.

We also calculated the energy differences between FM and AFM states of the perovskites. These differences are listed in Table 3. A negative (positive) value indicates that the AFM (FM) state is more stable. For both $LaMnO_3$ and $LaFeO_3$, the AFM ground state was reported experimentally[53,90]. Our FNDMC calculations reproduced the AFM ground state for both materials. For $LaFeO_3$, the functionals all reproduced the AFM ground state. SCAN agrees well with FNDMC (FMDMC: −0.08(1) vs. SCAN: −0.08 eV). However, none of the DFT functionals that we tested gave the AFM ground state for $LaMnO_3$.

Determining the magnetic ground state for $LaCoO_3$ is rather more complex than for $LaMnO_3$ and $LaFeO_3$ because different spin states of the cobalt ion are nearly degenerated. Here, we briefly discuss the main results of our previous work[16]. The ground state of bulk $LaCoO_3$, Co^{3+}, was reported experimentally in 1957 to be low spin (LS) $t_{2g}^6 e_g^0$ at low temperature (T<30 K) and therefore non-magnetic (NM)[91]. However, experiments in recent years have challenged this idea[92–96]. It is argued that at elevated temperatures, the LS Co^{3+} transitions into a high-spin/low-spin mixture; at temperatures above 500K, the ground state is completely high-spin (HS; $t_{2g}^4 e_g^2$) Co^{3+}[91]. In our FNDMC calculations, we found that the ground state of $LaCoO_3$ at 0 K is an HS AFM[16] state. Using FNDMC, the magnetic state energy ordering was revealed to be HS-AFM < HS/LS-FM < HS-FM < LS < intermediate spin-FM. The FNDMC total energy difference between the most and second-most stable states (i.e., HS-AFM and HS/LS-FM) was 0.15 eV, which indicates an HS-AFM ground state. Table 3 shows the energy differences of HS-AFM−HS/LS-FM. SCAN and LDA+U reproduce FNDMC; PBE does not.

From the above discussion, we conclude that FNDMC is better at evaluating the energies related to the perovskite systems. Therefore, we used FNDMC to evaluate the defect formation energies.

Local magnetization of point defects.
A point defect was introduced into the bulk supercell with the AFM ordering because this is the ground state of the bulk structures and we target the formation energy of an
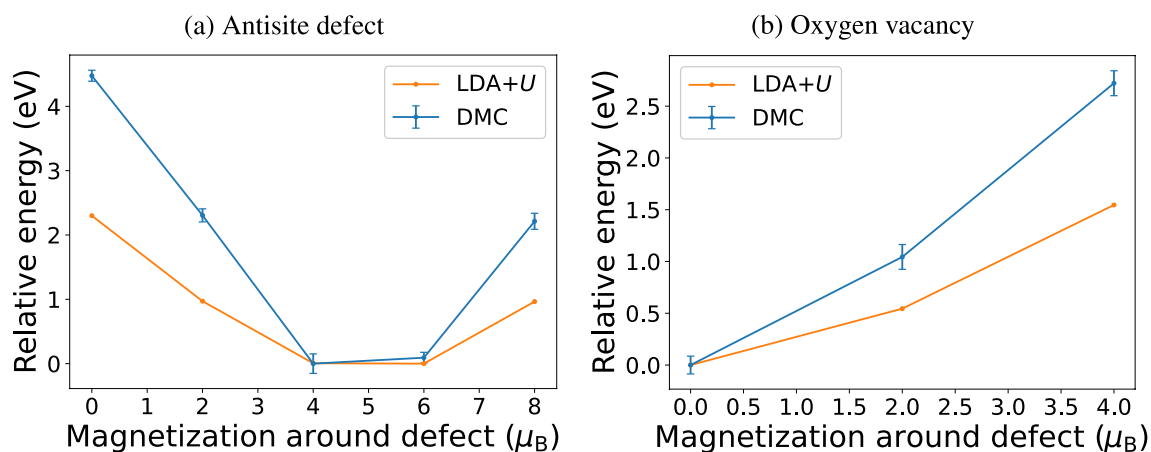
(a) Antisite defect

(b) Oxygen vacancy

Figure 2. (Color Online) Relative energies obtained with FNDMC (blue) and LDA+U (orange) calculations of LaMnO$_3$ with (**a**) antisite defect and (**b**) oxygen vacancy as a function of the total magnetization. The lowest data point is set to zero. LDA+U reproduces the defect magnetization (i.e., energy minima) of FNDMC.

isolated point defect. We optimized the magnetic moment around the point defect to minimize the total energy. Figure 2 shows the total energies of defects in LaMnO$_3$, antisite defects or oxygen vacancies, for different magnetic moments around the defect. The blue lines are the FNDMC results, and the orange lines are the LDA+U results. The total energies are shown as the relative differences from the lowest value. The minima of FNDMC and LDA+U agreed with each other. The antisite defect was magnetized by 4 or 6 μ_B in LaMnO$_3$, whereas the oxygen vacancy is not magnetized.

Because FNDMC and LDA+U agreed with each other in terms of the magnetization of point defects in LaMnO$_3$, we simply used LDA+U to determine the magnetization of defects used for the FNDMC calculations for LaFeO$_3$ and LaCoO$_3$. For LaFeO$_3$, we obtained 5 μ_B/defect for the antisite defect and 0 μ_B/defect for the oxygen vacancy. For LaCoO$_3$, we obtained 4 μ_B/defect for the antisite defect and 0 μ_B/defect for the oxygen vacancy. In all the perovskites, the transition metal antisite defects have finite local magnetizations, but the oxygen vacancy does not.

Relative abundance of antisite defects in LaMnO$_3$ and LaFeO$_3$. Figure 3 illustrates the main result of this research: the antisite defect and oxygen vacancy formation energies of LaMO$_3$ (M = Mn, Fe, and Co) for different chemical equilibrium conditions. In the case of LaMnO$_3$ and LaFeO$_3$, the antisite defect formation energies are almost always significantly lower than the oxygen vacancy formation energies. For LaMnO$_3$, a very small antisite defect formation energy (0.51(12) eV) was predicted at the chemical potentials, where MnO, MnO$_2$, and LaMnO$_3$ coexist. Similarly, in the case of LaFeO$_3$, the antisite formation energy at the O-poor condition limit, where LaFeO$_3$,Fe, and FeO coexist, was predicted to be almost zero (0.016(95) eV). The antisite defect formation energies in LaCoO$_3$ are always high (> 2.5 eV), and the formation of antisite defects at equilibrium appears to be very difficult. In summary, our results suggest possible antisite defect formation in LaMnO$_3$ and LaFeO$_3$ for M-rich and O-poor conditions because the formation energy appears to be much lower than the oxygen vacancy (Fig. 4) that is often reported in perovskite materials.

Table 4 summarizes the formation energies of the oxygen vacancy at the O-rich limit (i.e., $\mu_O = 0.5 \cdot E(O_2)$) obtained with different methods. Our FNDMC calculations nearly reproduced experimental estimates of the oxygen vacancy formation energies for LaMnO$_3$ and LaFeO$_3$. This corroborates the accuracy of our FNDMC calculations for defects. Among the DFT results, the PW91+U method also nearly reproduced the experimental results[97,98], but the others did not. These previous DFT calculations without the Hubbard U correction overestimated the oxygen vacancy formation energies for the LaMnO$_3$ case. The Hubbard U correction tends to decrease the vacancy formation energy. For the LaCoO$_3$ case, the previous DFT calculations with the Hubbard U correction all underestimated the oxygen vacancy formation energy compared to our FNDMC results.

Our FNDMC calculations suggested a relative abundance of antisite defects; however, no direct observations of antisite defects were found in the literature review. This lack could be due to the difficulty in observing these antisite defects. Because the transition metal atom has fewer electrons (25,26, and 27) than the La atom (57), the antisite defects would be masked by the La atom and cannot be easily observed in the transmission electron microscopy experiments. Similarly, x-ray diffraction experiments would not observe the antisite defects unless they are ordered. These reliable FNDMC results of antisite defects formation could accelerate their discovery in perovskites.

Atomic distortions around the antisite defect. Figure 5 shows the relaxed structure around the antisite defect in LaMO$_3$ (M=Mn, Fe, and Co). The antisite defect shifts from the original La site position towards some of the surrounding oxygen atoms. This is attributed to the significantly smaller ionic radii of Mn^{3+}, Fe^{3+}, and Co^{3+} (respectively 0.785, 0.785, and 0.75 Å) compared to that of La^{3+} (1.172 Å)[106]. Table 5 compares the distances between the antisite defect and surrounding O atoms with those between the La atom and surrounding O atoms in the bulk structure. This table clarifies that the antisite defect selectively bonds with some specific O
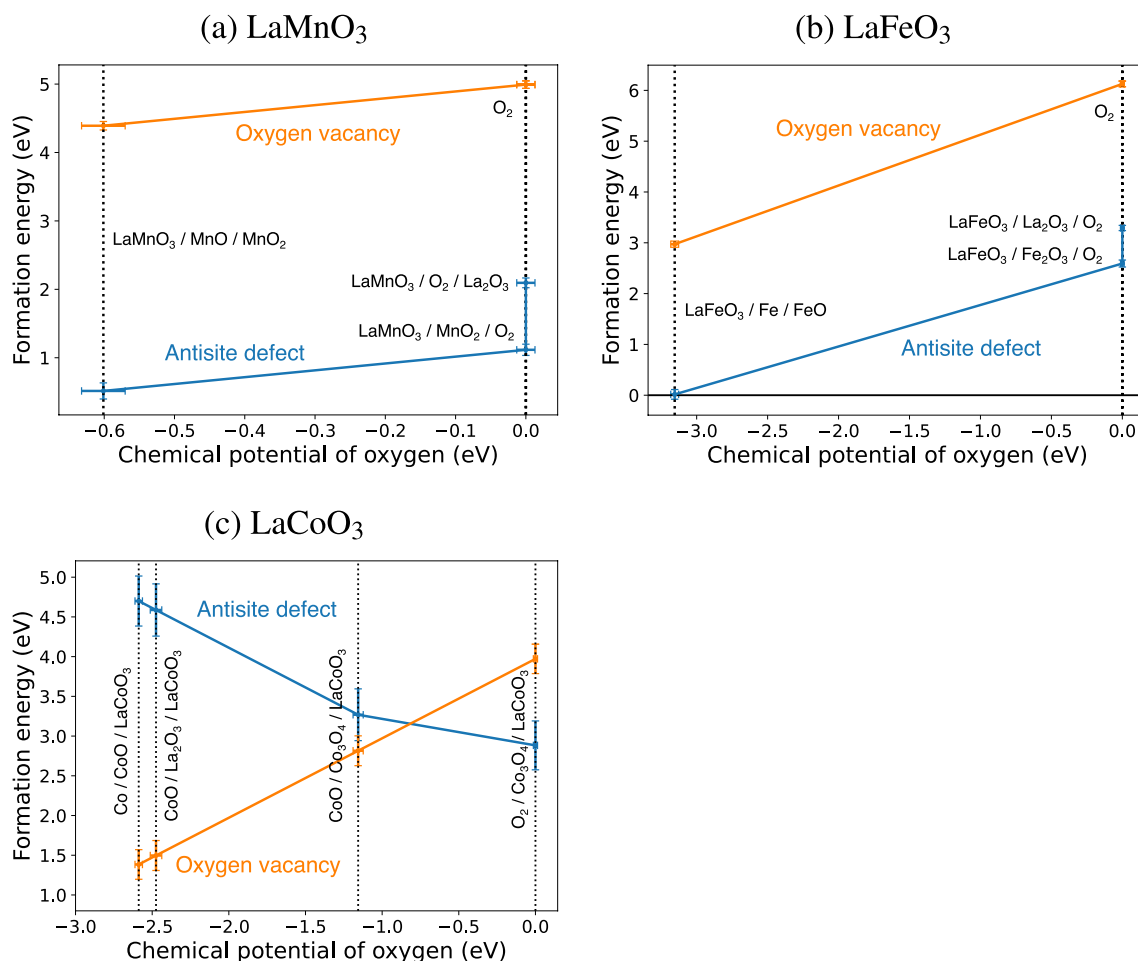
Figure 3. FNDMC prediction of the antisite defect and the oxygen vacancy formation energies as a function of O chemical potential for (**a**) LaMnO$_3$ (**b**) LaFeO$_3$, and (**c**) LaCoO$_3$. The vertical lines indicate the chemical potential where three compounds coexist.
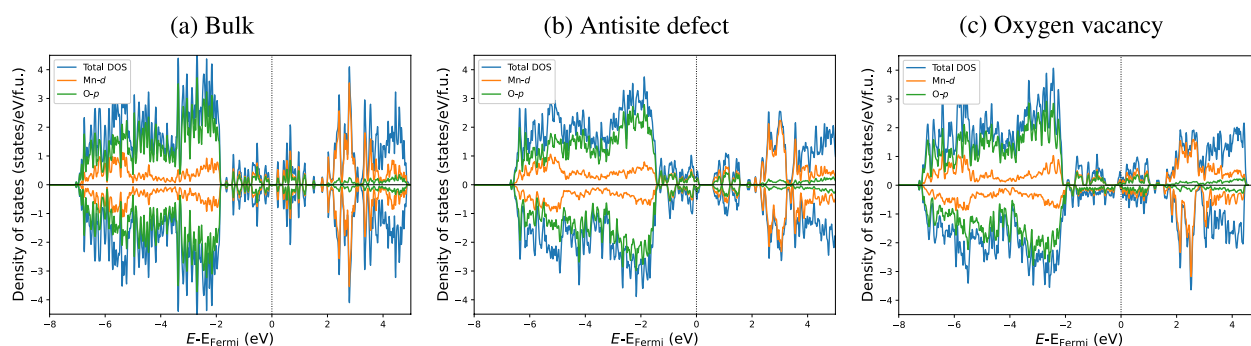

Figure 4. Density of states of LaMnO$_3$ with (**a**) no defects (bulk), (**b**) antisite defects, and (**c**) oxygen vacancies.

atoms compared to La atoms, because of the shorter ionic radius than La. The coordination numbers of O atoms around the antisite defect appears to be three for LaMnO$_3$ and LaFeO$_3$ and four for LaCoO$_3$ based on the listed distances.

We next discuss the formal charges of the antisite defects comparing the antisite–O distances and the antisite's coordination numbers with different transition metal (TM) oxides' TM–O distances and TM's coordination numbers. The TM–O distances and TM's coordination numbers are summarized in Table 6. The TM–O distances are smaller or TM's coordination number is larger when the TM's formal charge is larger. For the LaMnO$_3$ case, the antisite–O distances are slightly larger than the TM–O distances in the bulk LaMnO$_3$, and the antisite's coordination number is also smaller. Therefore, the antisite defect's formal charge is smaller than +3. For the LaFeO$_3$ case, whereas the antisite–O distances are shorter than the TM–O distances of bulk LaFeO$_3$ and Fe$_2$O$_3$, the antisite's coordination number is smaller. Therefore, the formal charge of the antisite defect cannot be decided

Reference	LaMnO$_3$	LaFeO$_3$	LaCoO$_3$
FNDMC	4.20 (5) eV	6.12 (6) eV	3.97 (19) eV
Expt.	3.6–4.1 eV[97,99,100]	4–6 eV[97,101]	–
PW91+U	3.6 eV[97,98]	4.1–4.5 eV[97,98]	2.7 eV[97,98]
PBE+U	–	–	2.23 eV[102]
LDA+U	3.14 eV[103]	–	3.07 eV[102]
PW91	4.7 eV[104]	–	–
PBE	~4.5 eV[105]	–	–

Table 4. Comparison of oxygen vacancy formation energies at the most O-rich condition.
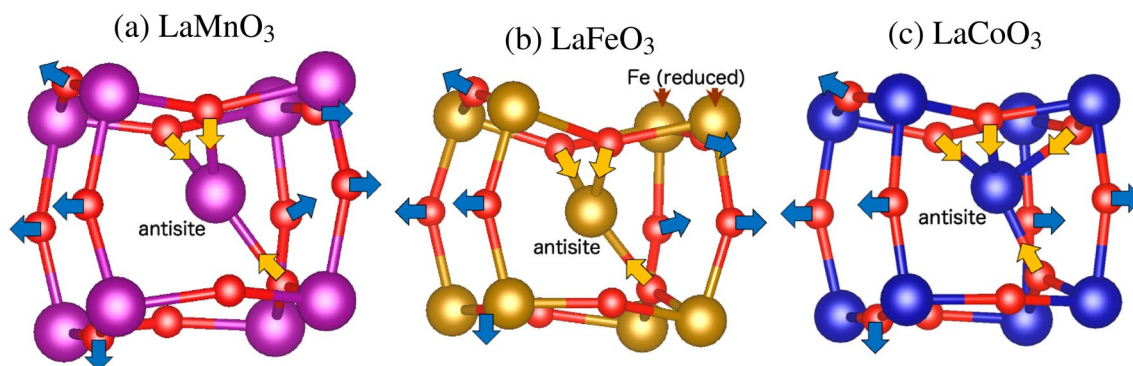
Figure 5. Atomic distortions around the antisite defect in LaMO$_3$ (M=Mn, Fe, and Co).

	LaMnO$_3$		LaFeO$_3$		LaCoO$_3$	
	La–O	Mn$_{La}$–O	La–O	Fe$_{La}$–O	La–O	Co$_{La}$–O
	2.427	2.051	2.395	1.915	2.409	1.849
	2.470	2.071	2.426	1.923	2.409	1.899
	2.470	2.089	2.426	1.923	2.409	1.935
$d_{bonding}$	2.546	2.450	2.526	2.592	2.768	1.966
	2.625	2.928	2.647	2.715	2.768	2.725
	2.625	2.945	2.647	3.072	2.768	2.822
d_{ionic}	2.57	2.19	2.57	2.19	2.57	2.15

Table 5. Bonding distances $d_{bonding}$ (Å) between La atom and surrounding O atoms in bulk LaMO$_3$ (left column) and antisite defect and surrounding O atoms in LaMO$_3$ (right column) for M = Mn, Fe, and Co, respectively. Up to the 6th shortest bonding distances are listed in ascending order. The bottom row indicates the sum of ionic radii d_{ionic} (Å) of the bonding ions: La^{3+} or M^{3+} and O^{2-}[106].

System	Q_{formal}	Q_{Bader}	TM-O distances (Å)
MnO	+ 2	+ 1.36	2.25($\times$6)
LaMnO$_3$	+ 3	+ 1.67	1.97($\times$2), 1.99($\times$2), 2.08($\times$2)
MnO$_2$	+ 4	+ 1.89	1.88($\times$6)
FeO	+ 2	+ 1.34	2.17($\times$6)
Fe$_2$O$_3$	+ 3	+ 1.84	1.93($\times$3), 2.14($\times$3)
LaFeO$_3$	+ 3	+ 1.81	2.00–2.02($\times$6)
CoO	+ 2	+ 1.21	+1.96($\times$4)
LaCoO$_3$	+ 3	+ 1.63	2.00($\times$6)

Table 6. The formal charges Q_{formal} and Bader charges Q_{Bader} of transition metal (TM) ion, distances between the TM and nearest O ions, and O coordination numbers around a TM ion in different transition metal oxides. The parenthesis value indicates the number of bonds of the bonding distance.

based on distances and coordination. Similarly, the antisite's formal charge in $LaCoO_3$ cannot be decided: the antisite–O distances are smaller than the TM–O distance in the bulk $LaCoO_3$ but the antisite's coordination number is smaller.

In order to estimate the formal charge of the antisite defects, we calculated their Bader charges[107–110] for the electronic densities given by LDA+U method. For the $LaMnO_3$ case, Mn atoms in the bulk structure have larger Bader charge (1.67 e) than the antisite defect's (1.43 e). This supports the discussion in the prior paragraph that the antisite defect's formal charge is smaller than +3. For the $LaFeO_3$ case, the antisite defect has the same Bader charge as the Fe atoms' in the bulk structure (1.78 e). However, the Fe atoms labeled "(reduced)" in Figure 5 have smaller Bader charges (1.59 e): their formal charges are smaller than +3. On the other hand, for the $LaCoO_3$ case, the antisite and the other Co ions have similar Bader charges to the Co atoms' in the bulk $LaCoO_3$.

The Bader charges of La atoms in the bulk $LaMO_3$ ($\sim$2.14 e) are significantly larger than the antisite defects'. Therefore, the antisite defects could disturb the local charge neutrality. Positively charged antisite defects could be more easily formed when the Fermi energy is lower. It remains to be investigated in the future how the antisite defect formation energies depend on the defect charge and Fermi energy. The neutral defects do not depend on the Fermi energy and are thus an upper bound for the formation energies of these defects. While very high or very low Fermi energies may lower the energies of charge defects below the neutral ones, the existence of charge defects will not change the main conclusion of this work since it can lower their formation energy further.

Defect's contributions to the density of states.   Figure 4 shows the PDOS of $LaMnO_3$ without defects, with antisite defects, and with oxygen vacancies. The PDOS of $LaFeO_3$ and $LaCoO_3$ are given in the SI. The total magnetizations were obtained in DFT, without the restriction used in FNDMC that constrains the magnetization value to be an integer. We obtained different total magnetization from the trial wave functions for $LaMnO_3$ with antisite defects (4→5.05 μ_B) and for $LaMnO_3$ with oxygen vacancies (0→0.15 μ_B). However, the energy differences were less than 0.016 eV/atom.

LDA+U with the optimal U values yielded by FNDMC reproduced earlier reports that the bulk $LaMO_3$ (M = Mn, Fe, and Co) are insulators. However, the $LaMnO_3$ band gap given by LDA+U was 0.08 eV, which is significantly smaller than the experimental values, 1.7 and 1.9 eV[111,112]. In our previous work, PBE+U also underestimated the band gap (0.2 eV) and FNDMC reasonably reproduced the experimental value (2.3(3) eV)[54]. DFT with a hybrid functional also gave 2.3 eV[113] so the Hubbard U correction alone would not be enough to obtain the band gaps of $LaMnO_3$. The $LaFeO_3$ band gap given by LDA+U was 2.77 eV, which is close to a reported value of 2.37 eV, which was produced by applying Tauc models to experimental data[114]. The $LaCoO_3$ band gap given by LDA+U in our work[16] was 1.94 eV, which is significantly larger than the experimental band gap of 0.5 eV[115,116]. However, these experiments reported a non-magnetic state, whereas we found the AFM state for a theoretical defect-free material. The reasons of disagreement between theory and experiments on the magnetic ground state of $LaCoO_3$ remains a subject of active research. Regarding the gap, we found that the band gap of the NM state of $LaCoO_3$ is 1.390 eV by LDA+U, which is closer to the experimental value.

Among the bulk structures, only $LaMnO_3$ has small density of states (DOS) around the Fermi energy, in agreement with an experiment[111]. They found that states exist around the Fermi level originating mainly from e_g orbitals of the d-shell in Mn. They also observed that a large splitting exists between t_{2g} and e_g orbitals, and a small splitting is also in the e_g orbitals. They explained that the small splitting is attributed to the Jahn–Teller distortions of the octahedral crystal field. Consequently, a significantly smaller band gap exists for $LaMnO_3$ than for the other two perovskites in our results. Our results show that point defects can turn $LaMnO_3$ metallic. Figure 4b and c indicate that antisite defects (oxygen vacancies) yield p-type (n-type) conductivity: antisite defects (oxygen vacancies) cause the Fermi energy to shift toward the valence (conduction) band. The shift of Fermi energy with charge neutral oxygen vacancies may be because of reduction of the system. Formation of +2 charged oxygen vacancies may inversely shift the Fermi energy toward the valence band. For $LaFeO_3$ and $LaCoO_3$, the antisite defects create defect energy levels in the band gap of the bulk structure. As a result, the band gap is reduced from 2.37 to 0.65 eV for $LaFeO_3$ and from 1.92 to 1.11 eV for $LaCoO_3$. The oxygen vacancies also narrow the band gap of $LaCoO_3$ from 1.92 to 1.12 eV and make $LaFeO_3$ conductive, producing an isolated DOS peak around the Fermi energy; the experimental disappearance or narrowing of the band gap could be evidence of formation of point defects.

Conclusion
We studied the charge neutral antisite defects and oxygen vacancy formation energies of $LaMO_3$ (M = Mn, Fe, and Co) by FNDMC. Our calculations predicted a relative abundance of antisite defects for the cases of M = Mn and Fe, comparable with or higher than the oxygen vacancies, at the M-rich and O-poor conditions.

The transition metal atoms studied have significantly fewer electrons (25, 26, and 27) than La (57). Therefore, the presence of antisite defects should be difficult to observe in transmission electron microscopy experiments because the presence of antisite defects would be masked by the La atoms on the same column. However, we found that antisite defects affect the electronic and magnetic properties of the perovskite host. Our PDOS analyses showed that the antisite defects make the $LaMnO_3$ metallic introducing holes and energy levels inside the band gap of $LaFeO_3$ and $LaCoO_3$. Mid gap levels could be a signal that antisite defects have formed in experiments. Our FNDMC calculations also showed that the antisite defects have local magnetization.

Data availability
The calculation data for the results in this study is available from the corresponding authors on request.

References

1. Chaloupka, J. & Khaliullin, G. Orbital order and possible superconductivity in LaNiO$_3$/LaMO$_3$ superlattices. *Phys. Rev. Lett.* **100**, 016404. https://doi.org/10.1103/PhysRevLett.100.016404 (2008).
2. Toulemonde, O. *et al.* Probing Co- and Fe-doped LaMO$_3$ (M = Ga, Al) perovskites as thermal sensors. *Dalton Trans.* **47**, 382–393. https://doi.org/10.1039/c7dt03647g (2018).
3. Islam, M. S., Slater, P. R. & Tolchard, J. R. Dinges T (2004) Doping and defect association in AZrO$_3$ (A = Ca, Ba) and LaMO$_3$ (M = Sc, Ga) perovskite-type ionic conductors. *Dalton Trans.* **19**, 3061–3066. https://doi.org/10.1039/b402669c (2004).
4. Arulraj, A. *et al.* Insulator-metal transitions, giant magnetoresistance, and related aspects of the cation-deficient LaMnO$_3$ compositions La$_{1−δ}$ MnO$_3$ and LaMn$_{1−δ'}$ O$_3$. *J. Solid State Chem.* **127**, 87–91. https://doi.org/10.1006/jssc.1996.0360 (1996).
5. Mahendiran, R. *et al.* Structure, electron-transport properties, and giant magnetoresistance of hole-doped LaMnO$_3$ systems. *Phys. Rev. B* **53**, 3348–3358. https://doi.org/10.1103/physrevb.53.3348 (1996).
6. Zhang, W., Zhuang, M., Xia, K. & Ming, N. A simple model of the giant magnetoresistance in doped LaMnO$_3$ perovskite. *Phys. Lett. A* **237**, 90–94. https://doi.org/10.1016/s0375-9601(97)00838-4 (1997).
7. Ji, Q., Bi, L., Zhang, J., Cao, H. & Zhao, X. S. The role of oxygen vacancies of ABO$_3$ perovskite oxides in the oxygen reduction reaction. *Energy Environ. Sci.* **13**, 1408–1428. https://doi.org/10.1039/d0ee00092b (2020).
8. Tho, N. D. *et al.* High temperature calcination for analyzing influence of 3d transition metals on gas sensing performance of mixed potential sensor Pt/YSZ/LaMO$_3$ (M = Mn, Fe Co, Ni). *Electrochim. Acta* **190**, 215–220. https://doi.org/10.1016/j.electacta.2015.12.205 (2016).
9. Sun, X., Zhang, C., Feng, T. & Jiang, D. Sensing behavior of mixed potential NO$_2$ sensors equipped with LaMO$_3$ (M = Fe or Cr) sensing electrodes. *Ionics* **21**, 1725–1730. https://doi.org/10.1007/s11581-014-1338-2 (2015).
10. Mathur, N. D. *et al.* Large low-field magnetoresistance in La$_{0.7}$ Ca$_{0.3}$ MnO$_3$ induced by artificial grain boundaries. *Nature* **387**, 266–268. https://doi.org/10.1038/387266a0 (1997).
11. Zhang, C. *et al.* LaMnO$_3$ perovskites via a facile nickel substitution strategy for boosting propane combustion performance. *Ceram. Int.* **46**, 6652–6662. https://doi.org/10.1016/j.ceramint.2019.11.153 (2020).
12. Li, Z. et al. An effective method for enhancing oxygen evolution kinetics of LaMO$_3$ (M = Ni, Co, Mn) perovskite catalysts and its application to a rechargeable zinc-air battery. *Appl. Catal. B: Environ.* **262**, https://doi.org/10.1016/j.apcatb.2019.118291 (2020).
13. Nolting, F. *et al.* Direct observation of the alignment of ferromagnetic spins by antiferromagnetic spins. *Nature* **405**, 767–769. https://doi.org/10.1038/35015515 (2000).
14. Schlom, D. G., Chen, L.-Q., Pan, X., Schmehl, A. & Zurbuchen, M. A. A thin film approach to engineering functionality into oxides. *J. Am. Ceram. Soc.* **91**, 2429–2454. https://doi.org/10.1111/j.1551-2916.2008.02556.x (2008).
15. Christen, H. M. & Eres, G. Recent advances in pulsed-laser deposition of complex oxides. *J. Phys.: Condens. Matter* **20**, 264005. https://doi.org/10.1088/0953-8984/20/26/264005 (2008).
16. Saritas, K., Krogel, J. T., Okamoto, S., Lee, H. N. & Reboredo, F. A. Structural, electronic, and magnetic properties of bulk and epitaxial LaCoO$_3$ through diffusion Monte Carlo. *Phys. Rev. Mater.* **3**, 124414. https://doi.org/10.1103/PhysRevMaterials.3.124414 (2019).
17. Hosoda, M., Bell, C., Hikita, Y. & Hwang, H. Y. Compositional and gate tuning of the interfacial conductivity in LaAlO$_3$/LaTiO$_3$/SrTiO$_3$ heterostructures. *Appl. Phys. Lett.* **102**, 091601. https://doi.org/10.1063/1.4794410 (2013).
18. Song, G. & Zhang, W. First-principles study on the phase diagram and multiferroic properties of (SrCoO$_3$)$_1$/(SrTiO$_3$)$_1$ superlattices. *Sci. Rep.* **4**, 1–6. https://doi.org/10.1038/srep04564 (2014).
19. Petrie, J. R. *et al.* Strain control of oxygen vacancies in epitaxial strontium cobaltite films. *Adv. Funct. Mater.* **26**, 1564–1570. https://doi.org/10.1002/adfm.201504868 (2016).
20. Biscaras, J. *et al.* Two-dimensional superconductivity at a Mott insulator/band insulator interface LaTiO$_3$/SrTiO$_3$. *Nat. Commun.* **1**, 89. https://doi.org/10.1038/ncomms1084 (2010).
21. Reyren, N. *et al.* Superconducting interfaces between insulating oxides. *Science* **317**, 1196–1199. https://doi.org/10.1126/science.1146006 (2007).
22. Ji, Q., Bi, L., Zhang, J., Cao, H. & Zhao, X. S. The role of oxygen vacancies of ABO$_3$ perovskite oxides in the oxygen reduction reaction. *Energy Environ. Sci.* **13**, 1408–1428. https://doi.org/10.1039/D0EE00092B (2020).
23. Yoo, J. S., Liu, Y., Rong, X. & Kolpak, A. M. Electronic origin and kinetic feasibility of the lattice oxygen participation during the oxygen evolution reaction on perovskites. *J. Phys. Chem. Lett.* **9**, 1473–1479. https://doi.org/10.1021/acs.jpclett.8b00154 (2018).
24. Cheng, J., Navrotsky, A., Zhou, X.-D. & Anderson, H. U. Enthalpies of formation of LaMO$_3$ perovskites (M = Cr, Fe Co, and Ni). *J. Mater. Res.* **20**, 191–200. https://doi.org/10.1557/JMR.2005.0018 (2005).
25. Khan, M. S., Islam, M. S. & Bates, D. R. Dopant substitution and ion migration in the LaGaO$_3$-based oxygen ion conductor. *J. Phys. Chem. B* **102**, 3099–3104. https://doi.org/10.1021/jp972819d (1998).
26. Singh, D. J. Antisite defects and traps in perovskite YAlO$_3$ and LuAlO$_3$: density functional calculations. *Phys. Rev. B* **76**, 214115. https://doi.org/10.1103/PhysRevB.76.214115 (2007).
27. Polfus, J. M. *et al.* Solubility of transition metal interstitials in proton conducting BaZrO$_3$ and similar perovskite oxides. *J. Mater. Chem. A* **4**, 8105–8112. https://doi.org/10.1039/C6TA02377K (2016).
28. Han, D., Kishida, K., Shinoda, K., Inui, H. & Uda, T. A comprehensive understanding of structure and site occupancy of Y in Y-doped BaZrO$_3$. *J. Mater. Chem. A* **1**, 3027–3033. https://doi.org/10.1039/C2TA00675H (2013).
29. Becke, A. D. Perspective: fifty years of density-functional theory in chemical physics. *J. Chem. Phys.* **140**, 18A301. https://doi.org/10.1063/1.4869598 (2014).
30. Dudarev, S. L., Botton, G. A., Savrasov, S. Y., Humphreys, C. J. & Sutton, A. P. Electron-energy-loss spectra and the structural stability of nickel oxide: An LSDA+U study. *Phys. Rev. B* **57**, 1505–1509. https://doi.org/10.1103/PhysRevB.57.1505 (1998).
31. Grimm, R. & Storer, R. Monte-Carlo solution of Schrödinger's equation. *J. Comput. Phys.* **7**, 134–156. https://doi.org/10.1016/0021-9991(71)90054-4 (1971).
32. Anderson, J. B. Quantum chemistry by random walk. H^{2}P, H$_3^+$D$_{3h}^1$A$_1'$, H$_2^3$Σ$_u^+$, H$_4^1$Σ$_g^+$, Be^{1}S. *J. Chem. Phys.* **65**, 4121–4127. https://doi.org/10.1063/1.432868 (1976).
33. Trail, J., Monserrat, B., López Ríos, P., Maezono, R. & Needs, R. J. Quantum Monte Carlo study of the energetics of the rutile, anatase, brookite, and columbite TiO$_2$ polymorphs. *Phys. Rev. B* **95**, 121108. https://doi.org/10.1103/PhysRevB.95.121108 (2017).
34. Ichibha, T., Hou, Z., Hongo, K. & Maezono, R. New insight into the ground state of FePc: A diffusion Monte Carlo study. *Sci. Rep.* **7**, 2011. https://doi.org/10.1038/s41598-017-01668-6 (2017).
35. Ichibha, T., Benali, A., Hongo, K. & Maezono, R. Ti interstitial flows giving rutile TiO$_2$ reoxidation process enhancement in (001) surface. *Phys. Rev. Mater.* **3**, 125801. https://doi.org/10.1103/PhysRevMaterials.3.125801 (2019).
36. Luo, Y. *et al.* Phase stability of TiO$_2$ polymorphs from diffusion Quantum Monte Carlo. *New J. Phys.* **18**, 113049 (2016).
37. Ganesh, P. *et al.* Doping a bad metal: Origin of suppression of the metal-insulator transition in nonstoichiometric VO$_2$. *Phys. Rev. B* **101**, 155129. https://doi.org/10.1103/PhysRevB.101.155129 (2020).

38. Mitra, C., Krogel, J. T., Santana, J. A. & Reboredo, F. A. Many-body ab initio diffusion quantum Monte Carlo applied to the strongly correlated oxide NiO. *J. Chem. Phys.* **143**, 164710. https://doi.org/10.1063/1.4934262 (2015).

39. Lu, Q. et al. Metal–insulator transition tuned by oxygen vacancy migration across TiO_2/VO_2 interface. *Sci. Rep.* **10**, https://doi.org/10.1038/s41598-020-75695-1 (2020).

40. Bennett, M. C. *et al.* Origin of metal-insulator transitions in correlated perovskite metals. *Phys. Rev. Res.* **4**, L022005. https://doi.org/10.1103/PhysRevResearch.4.L022005 (2022).

41. Foyevtsova, K. *et al.* Ab initio quantum Monte Carlo calculations of spin superexchange in cuprates: The benchmarking case of Ca_2CuO_3. *Phys. Rev. X* **4**, 031003. https://doi.org/10.1103/PhysRevX.4.031003 (2014).

42. Wrobel, F. *et al.* Local structure of potassium doped nickel oxide: A combined experimental-theoretical study. *Phys. Rev. Mater.* **3**, 115003. https://doi.org/10.1103/PhysRevMaterials.3.115003 (2019).

43. Kylänpää, I., Luo, Y., Heinonen, O., Kent, P. R. C. & Krogel, J. T. Compton profile of VO_2 across the metal-insulator transition: Evidence of a non-Fermi liquid metal. *Phys. Rev. B* **99**, 075154. https://doi.org/10.1103/PhysRevB.99.075154 (2019).

44. Szyniszewski, M., Mostaani, E., Drummond, N. D. & Fal'ko, V. I. Binding energies of trions and biexcitons in two-dimensional semiconductors from diffusion quantum Monte Carlo calculations. *Phys. Rev. B* **95**, 081301. https://doi.org/10.1103/PhysRevB.95.081301 (2017).

45. Ertekin, E., Wagner, L. K. & Grossman, J. C. Point-defect optical transitions and thermal ionization energies from quantum Monte Carlo methods: Application to the *F*-center defect in MgO. *Phys. Rev. B* **87**, 155210. https://doi.org/10.1103/PhysRevB.87.155210 (2013).

46. Yu, J., Wagner, L. K. & Ertekin, E. Fixed-node diffusion Monte Carlo description of nitrogen defects in zinc oxide. *Phys. Rev. B* **95**, 075209. https://doi.org/10.1103/PhysRevB.95.075209 (2017).

47. Busemeyer, B., MacDougall, G. J. & Wagner, L. K. Prediction for the singlet-triplet excitation energy for the spinel $MgTi_2O_4$ using first-principles diffusion Monte Carlo. *Phys. Rev. B* **99**, 081118. https://doi.org/10.1103/PhysRevB.99.081118 (2019).

48. Yu, J., Wagner, L. K. & Ertekin, E. Fixed-node diffusion Monte Carlo description of nitrogen defects in zinc oxide. *Phys. Rev. B* **95**, 075209. https://doi.org/10.1103/PhysRevB.95.075209 (2017).

49. Fumanal, M., Wagner, L. K., Sanvito, S. & Droghetti, A. Diffusion Monte Carlo perspective on the spin-state energetics of $[Fe(NCH)_6]^{2+}$. *J. Chem. Theory Comput.* **12**, 4233–4241, https://doi.org/10.1021/acs.jctc.6b00332 (2016). PMID: 27500854.

50. Doblhoff-Dier, K., Meyer, J., Hoggan, P. E., Kroes, G.-J. & Wagner, L. K. Diffusion Monte Carlo for accurate dissociation energies of 3*d* transition metal containing molecules. *J. Chem. Theory Comput.* **12**, 2583–2597. https://doi.org/10.1021/acs.jctc.6b00160 (2016). PMID: 27175914.

51. Schrön, A., Rödl, C. & Bechstedt, F. Energetic stability and magnetic properties of MnO in the rocksalt, wurtzite, and zinc-blende structures: Influence of exchange and correlation. *Phys. Rev. B* **82**, 165109. https://doi.org/10.1103/PhysRevB.82.165109 (2010).

52. Scarel, G. *et al.* Vibrational and electrical properties of hexagonal La_2O_3 films. *Appl. Phys. Lett.* **91**, 102901. https://doi.org/10.1063/1.2779108 (2007).

53. Rodríguez-Carvajal, J. *et al.* Neutron-diffraction study of the Jahn–Teller transition in stoichiometric $LaMnO_3$. *Phys. Rev. B* **57**, R3189–R3192. https://doi.org/10.1103/PhysRevB.57.R3189 (1998).

54. Saritas, K., Krogel, J. T., Kent, P. R. C. & Reboredo, F. A. Diffusion Monte Carlo: A pathway towards an accurate theoretical description of manganese oxides. *Phys. Rev. Mater.* **2**, 085801. https://doi.org/10.1103/PhysRevMaterials.2.085801 (2018).

55. Peng, H. & Lany, S. Polymorphic energy ordering of MgO, ZnO, GaN, and MnO within the random phase approximation. *Phys. Rev. B* **87**, 174113. https://doi.org/10.1103/PhysRevB.87.174113 (2013).

56. Taguchi, H., Masunaga, Y., Hirota, K. & Yamaguchi, O. Synthesis of perovskite-type $(La_{1-x} Ca_x)FeO_3$ ($0 \leq x \leq 0.2$) at low temperature. *Mater. Res. Bull.* **40**, 773 – 780. https://doi.org/10.1016/j.materresbull.2005.02.009 (2005).

57. Marezio, M. & Dernier, P. The bond lengths in $LaFeO_3$. *Mater. Res. Bull.* **6**, 23–29. https://doi.org/10.1016/0025-5408(71)90155-3 (1971).

58. Lubarda, V. On the effective lattice parameter of binary alloys. *Mech. Mater.* **35**, 53–68. https://doi.org/10.1016/S0167-6636(02)00196-5 (2003).

59. McCammon, C. A. & Gun Liu, L. The effects of pressure and temperature on nonstoichiometric wüstite, Fe_xO: The iron-rich phase boundary. *Phys. Chem. Miner.* **10**, 106–113. https://doi.org/10.1007/bf00309644 (1984).

60. Maslen, E. N., Streltsov, V. A., Streltsova, N. R. & Ishizawa, N. Synchrotron X-ray study of the electron density in α-Fe_2O_3. *Acta Crystallogr. B* **50**, 435–441. https://doi.org/10.1107/S0108768194002284 (1994).

61. Xu, S., Habib, A. H., Gee, S. H., Hong, Y. K. & McHenry, M. E. Spin orientation, structure, morphology, and magnetic properties of hematite nanoparticles. *J. Appl. Phys.* **117**, 17A315. https://doi.org/10.1063/1.4914059 (2015).

62. The Materials Project. Materials Data on La_2O_3 (mp-2292) by Materials Project. https://doi.org/10.17188/1199085 (2020).

63. The Materials Project. Materials Data on Co (mp-54) by Materials Project. https://doi.org/10.17188/1263614 (2020).

64. The Materials Project. Materials Data on CoO (mp-22408) by Materials Project (2021).

65. The Materials Project. Materials Data on Co_3O_4 (mp-18748) by Materials Project. https://doi.org/10.17188/1193429 (2020).

66. The Materials Project. Materials Data on $LaCoO_3$ (mp-19051) by Materials Project. https://doi.org/10.17188/1193834 (2020).

67. Kresse, G. & Furthmüller, J. Efficient iterative schemes for ab initio total-energy calculations using a plane-wave basis set. *Phys. Rev. B* **54**, 11169–11186. https://doi.org/10.1103/PhysRevB.54.11169 (1996).

68. Perdew, J. P., Burke, K. & Ernzerhof, M. Generalized gradient approximation made simple. *Phys. Rev. Lett.* **77**, 3865–3868. https://doi.org/10.1103/PhysRevLett.77.3865 (1996).

69. Kresse, G. & Joubert, D. From ultrasoft pseudopotentials to the projector augmented-wave method. *Phys. Rev. B* **59**, 1758–1775. https://doi.org/10.1103/PhysRevB.59.1758 (1999).

70. Sun, J., Ruzsinszky, A. & Perdew, J. P. Strongly constrained and appropriately normed semilocal density functional. *Phys. Rev. Lett.* **115**, 036402. https://doi.org/10.1103/PhysRevLett.115.036402 (2015).

71. Kim, J. *et al.* QMCPACK: An open source ab initio quantum Monte Carlo package for the electronic structure of atoms, molecules and solids. *J. Phys. Condens. Matter* **30**, 195901. https://doi.org/10.1088/1361-648x/aab9c3 (2018).

72. Kent, P. R. C. *et al.* QMCPACK: Advances in the development, efficiency, and application of auxiliary field and real-space variational and diffusion quantum Monte Carlo. *J. Chem. Phys.* **152**, 174105. https://doi.org/10.1063/5.0004860 (2020).

73. Krogel, J. T. Nexus: A modular workflow management system for quantum simulation codes. *Comput. Phys. Commun.* **198**, 154–168. https://doi.org/10.1016/j.cpc.2015.08.012 (2016).

74. Foulkes, W. M. C., Mitas, L., Needs, R. J. & Rajagopal, G. Quantum Monte Carlo simulations of solids. *Rev. Mod. Phys.* **73**, 33–83. https://doi.org/10.1103/RevModPhys.73.33 (2001).

75. Santana, J. A., Krogel, J. T., Kent, P. R. C. & Reboredo, F. A. Diffusion quantum Monte Carlo calculations of $SrFeO_3$ and $LaFeO_3$. *J. Chem. Phys.* **147**, 034701. https://doi.org/10.1063/1.4994083 (2017).

76. Giannozzi, P. *et al.* QUANTUM ESPRESSO: A modular and open-source software project for quantum simulations of materials. *J. Phys.: Condens. Matter* **21**, 395502. https://doi.org/10.1088/0953-8984/21/39/395502 (2009).

77. Krogel, J. T. & Kent, P. R. C. Magnitude of pseudopotential localization errors in fixed node diffusion quantum Monte Carlo. *J. Chem. Phys.* **146**, 244101. https://doi.org/10.1063/1.4986951 (2017).

78. Kylänpää, I., Luo, Y., Heinonen, O., Kent, P. R. C. & Krogel, J. T. Compton profile of VO_2 across the metal-insulator transition: Evidence of a non-Fermi liquid metal. *Phys. Rev. B* **99**, 075154. https://doi.org/10.1103/PhysRevB.99.075154 (2019).

79. Annaberdiyev, A., Melton, C. A., Wang, G. & Mitas, L. Electronic structure of $\alpha - RuCl_3$ by fixed-node and fixed-phase diffusion Monte Carlo methods (2022). arXiv:2203.15949.

80. Chase, M. W. J. *NIST-JANAF Thermochemical Tables* (American Institute of Physics, 1998).

81. Solovʹev, S. N., Dupal, A. Y. & Shatalov, K. I. Standard enthalpy of formation of $LaCoO_3(cr)$. *Russ. J. Phys. Chem.* **80**, 2049–2050. https://doi.org/10.1134/s0036024406120314 (2006).

82. Cheng, J., Navrotsky, A., Zhou, X.-D. & Anderson, H. U. Thermochemistry of $La_{1-x} Sr_x FeO_{3-\delta}$ solid solutions (0.0 ≤ x ≤ 1.0, 0.0 ≤δ≤ 0.5). *Chem. Mater.* **17**, 2197–2207. https://doi.org/10.1021/cm048613o (2005).

83. Kittel, C. *Introduction to Solid State Physics* 8 edn (Wiley, 2004).

84. Catti, M., Valerio, G. & Dovesi, R. Theoretical study of electronic, magnetic, and structural properties of α-Fe_2O_3 (hematite). *Phys. Rev. B* **51**, 7441–7450. https://doi.org/10.1103/PhysRevB.51.7441 (1995).

85. Rodríguez-Carvajal, J. *et al.* Neutron-diffraction study of the Jahn–Teller transition in stoichiometric. *Phys. Rev. B Conden. Matter Mater. Phys.* **57**, R3189–R3192. https://doi.org/10.1103/PhysRevB.57.R3189 (1998).

86. Harrison, W. A. Tight-binding theory of manganese and iron oxides. *Phys. Rev. B* **77**, 245103. https://doi.org/10.1103/PhysRevB.77.245103 (2008).

87. of Japan, T. C. S. *Handbook of Chemistry: Pure Chemistry* 5th ed (Maruzen Publishing Co. Ltd., 2004).

88. Jog, K. N., Singh, R. K. & Sanyal, S. P. Phase transition and high-pressure behavior of divalent metal oxides. *Phys. Rev. B* **31**, 6047–6057. https://doi.org/10.1103/PhysRevB.31.6047 (1985).

89. Glasser, L. & Sheppard, D. A. Cohesive energies and enthalpies: Complexities, confusions, and corrections. *Inorg. Chem.* **55**, 7103–7110. https://doi.org/10.1021/acs.inorgchem.6b01056 (2016). PMID: 27362373.

90. Janbutrach, Y., Hunpratub, S. & Swatsitang, E. Ferromagnetism and optical properties of $La_{1-x} Al_x FeO_3$ nanopowders. *Nanoscale Res. Lett.* **9**, 498. https://doi.org/10.1186/1556-276X-9-498 (2014).

91. Koehler, W. C. & Wollan, E. O. Neutron-diffraction study of the magnetic properties of perovskite-like compounds $LaBO_3$. *J. Phys. Chem. Solids* **2**, 100–106. https://doi.org/10.1016/0022-3697(57)90095-1 (1957).

92. Belanger, D. P. *et al.* Structure and magnetism in $LaCoO_3$. *J. Phys.: Condens. Matter* **28**, 025602. https://doi.org/10.1088/0953-8984/27/12/126001 (2016).

93. Durand, A. M. *et al.* The unusual magnetism of nanoparticle $LaCoO_3$. *J. Phys.: Condens. Matter* **27**, 176003. https://doi.org/10.1088/0953-8984/27/17/176003 (2015).

94. Durand, A. M. *et al.* The effects of $Co_3 O_4$ on the structure and unusual magnetism of $LaCoO_3$. *J. Phys.: Condens. Matter* **27**, 126001–13. https://doi.org/10.1088/0953-8984/27/12/126001 (2015).

95. Kaminsky, G. M. *et al.* Origin of the net magnetic moment in $LaCoO_3$. *Phys. Rev. B* **97**, 024418. https://doi.org/10.1103/PhysRevB.97.024418 (2018).

96. Durand, A. M. *et al.* Magnetism and phase transitions in $LaCoO_3$. *J. Phys.: Condens. Matter* **25**, 382203. https://doi.org/10.1088/0953-8984/25/38/382203 (2013).

97. Kuklja, M. M., Kotomin, E. A., Merkle, R., Mastrikov, Y. A. & Maier, J. Combined theoretical and experimental analysis of processes determining cathode performance in solid oxide fuel cells. *Phys. Chem. Chem. Phys.* **15**, 5443–5471. https://doi.org/10.1039/C3CP44363A (2013).

98. Lee, Y.-L., Kleis, J., Rossmeisl, J. & Morgan, D. Ab initio energetics of La BO_3(001) ($B =$ Mn, Fe Co, and Ni) for solid oxide fuel cell cathodes. *Phys. Rev. B* **80**, 224101. https://doi.org/10.1103/PhysRevB.80.224101 (2009).

99. van Roosmalen, J. & Cordfunke, E. The defect chemistry of $LaMnO_{3+\delta}$: 5 thermodynamics. *J. Solid State Chem.* **110**, 113–117. https://doi.org/10.1006/jssc.1994.1144 (1994).

100. Zuev, A. & Tsvetkov, D. Oxygen nonstoichiometry, defect structure and defect-induced expansion of undoped perovskite $LaMnO_{3\pm\delta}$. *Solid State Ionics* **181**, 557–563. https://doi.org/10.1016/j.ssi.2010.02.024 (2010).

101. Mizusaki, J., Yoshihiro, M., Yamauchi, S. & Fueki, K. Nonstoichiometry and defect structure of the perovskite-type oxides $La_{1-x} Sr_x FeO_{3-\delta}$. *J. Solid State Chem.* **58**, 257–266. https://doi.org/10.1016/0022-4596(85)90243-9 (1985).

102. Ritzmann, A. M., Pavone, M., Muñoz-García, A. B., Keith, J. A. & Carter, E. A. Ab initio DFT+U analysis of oxygen transport in $LaCoO_3$: the effect of Co^{3+} magnetic states. *J. Mater. Chem. A* **2**, 8060–8074. https://doi.org/10.1039/c4ta00801d (2014).

103. Olsson, E., Aparicio-Anglès, X. & de Leeuw, N. H. Ab initio study of vacancy formation in cubic $LaMnO_3$ and $SmCoO_3$ as cathode materials in solid oxide fuel cells. *J. Chem. Phys.* **145**, 014703. https://doi.org/10.1063/1.4954939 (2016).

104. Kotomin, E. A., Mastrikov, Y. A., Heifets, E. & Maier, J. Adsorption of atomic and molecular oxygen on the $LaMnO_3$ (001) surface: Ab initio supercell calculations and thermodynamics. *Phys. Chem. Chem. Phys.* **10**, 4644–4649. https://doi.org/10.1039/B804378G (2008).

105. Mastrikov, Y. A., Merkle, R., Kotomin, E. A., Kuklja, M. & Maier, J. Surface termination effects on the oxygen reduction reaction rate at fuel cell cathodes. *J. Mater. Chem. A* **6**, 11929–11940. https://doi.org/10.1039/C8TA02058B (2018).

106. Shannon, R. D. Revised effective ionic radii and systematic studies of interatomic distances in halides and chalcogenides. *Acta Crystallogr. A* **32**, 751–767. https://doi.org/10.1107/S0567739476001551 (1976).

107. Yu, M. & Trinkle, D. R. Accurate and efficient algorithm for Bader charge integration. *J. Chem. Phys.* **134**, 064111. https://doi.org/10.1063/1.3553716 (2011).

108. Tang, W., Sanville, E. & Henkelman, G. A grid-based Bader analysis algorithm without lattice bias. *J. Phys.: Condens. Matter* **21**, 084204. https://doi.org/10.1088/0953-8984/21/8/084204 (2009).

109. Henkelman, G., Arnaldsson, A. & Jónsson, H. A fast and robust algorithm for Bader decomposition of charge density. *Comput. Mater. Sci.* **36**, 354–360. https://doi.org/10.1016/j.commatsci.2005.04.010 (2006).

110. Sanville, E., Kenny, S. D., Smith, R. & Henkelman, G. Improved grid-based algorithm for Bader charge allocation. *J. Comput. Chem.* **28**, 899–908. https://doi.org/10.1002/jcc.20575 (2007).

111. Saitoh, T. *et al.* Electronic structure of $La_{1-x}Sr_x MnO_3$ studied by photoemission and x-ray-absorption spectroscopy. *Phys. Rev. B* **51**, 13942–13951. https://doi.org/10.1103/PhysRevB.51.13942 (1995).

112. Jung, J. H. *et al.* Determination of electronic band structures of $CaMnO_3$ and $LaMnO_3$ using optical-conductivity analyses. *Phys. Rev. B* **55**, 15489–15493. https://doi.org/10.1103/PhysRevB.55.15489 (1997).

113. Piskunov, S., Spohr, E., Jacob, T., Kotomin, E. A. & Ellis, D. E. Electronic and magnetic structure of $La_{0.875}Sr_{0.125}MnO_3$ calculated by means of hybrid density-functional theory. *Phys. Rev. B* **76**, 012410. https://doi.org/10.1103/PhysRevB.76.012410 (2007).

114. Scafetta, M. D., Cordi, A. M., Rondinelli, J. M. & May, S. J. Band structure and optical transitions in $LaFeO_3$: theory and experiment. *J. Phys.: Condens. Matter* **26**, 505502. https://doi.org/10.1088/0953-8984/26/50/505502 (2014).

115. Ma, C.-L. & Cang, J. First principles investigation on the band gap of the ground state of $LaCoO_3$. *Solid State Commun.* **150**, 1983–1986. https://doi.org/10.1016/j.ssc.2010.08.023 (2010).

116. Chainani, A., Mathew, M. & Sarma, D. D. Electron-spectroscopy study of the semiconductor-metal transition in $La_{1-x} Sr_x CoO_3$. *Phys. Rev. B* **46**, 9976–9983. https://doi.org/10.1103/PhysRevB.46.9976 (1992).

Acknowledgements

Author contributions

T.I., K.S., J.K., and F.R. conceived the idea. T.I. and K.S. performed the calculations. J.K., Y.L., and P.K. developed the code and supported the calculations. F.R. supervised the work. All authors contributed to the discussion and writing of the paper.

Competing Interests

The authors declare no competing interests.

Additional information

Supplementary Information The online version contains supplementary material available at https://doi.org/10.1038/s41598-023-33578-1.

Correspondence and requests for materials should be addressed to T.I. or F.A.R.

Reprints and permissions information is available at www.nature.com/reprints.

Publisher's note Springer Nature remains neutral with regard to jurisdictional claims in published maps and institutional affiliations.